

Estimation of Gravitational Wave from Solar Emerging Magnetic Flux Tube

Siqi Guan^{1,2}, Shangbin Yang^{1,2}, and Xiao Guo³

Received 2025 July 30; revised 2025 September 23; accepted 2025 October 10; published 2025 November 17

Abstract

This study investigates the gravitational waves (GWs) generated by the emergence of magnetic flux tubes in the solar convection zone. We focus on the upward buoyancy of magnetic flux tubes, which leads to significant magnetic activity and the formation of active region sunspots. This study adopts parameters representative of a moderate-sized solar active region to estimate the GWs generated by the emergence of magnetic flux tubes. Our results indicate that the GW strain amplitude, achievable through signal superposition and detection at close proximity (e.g., approximately one solar radius from the solar surface), may reach $\sim 10^{-29}$. The characteristic GW frequency is estimated at $\sim 10^{-5}$ Hz, placing it at the high-frequency end of the sensitivity band of Pulsar Timing Array (PTA) methods. However, the estimated strain amplitudes remain orders of magnitude below the sensitivity thresholds of current and foreseeable GW detectors. Notably, reducing the cadence Δt of PTA observations to approximately 2 hr ($\Delta t = 2$ hr) would raise the maximum detectable frequency to about 5.8 \times 10⁻⁵ Hz, thereby encompassing the dominant spectral component of solar activity-related GWs predicted in this study, offering a potential pathway for future detection. Successful detection in the future may help to predict the super solar active region emergence in space weather forecasting.

Key words: acceleration of particles – gravitational waves – methods: analytical – Sun: activity

1. Introduction

The solar convection zone governs the Sun's magnetic activity, significantly influencing space weather and stellar physics. Gizon & Birch (2005) challenge traditional buoyant flux tube models by demonstrating how toroidal fields rise to form active regions, underscoring the need to probe magnetic dynamics in this critical layer. This research emphasizes the importance of studying the solar structure and the role of magnetic fields in solar activity, highlighting the need for continued investigation into the solar convection zone's magnetic dynamics. To probe these complex dynamics deep within the Sun, researchers have historically relied on two primary methods: the historical exploration of the Sun's interior has primarily utilized helioseismology and solar neutrino observations. Helioseismology, through the analysis of solar oscillations, has been instrumental in mapping the Sun's interior structure (Fan 2021). Solar neutrinos, detected through various experiments, have provided direct evidence of the nuclear reactions occurring within the Sun's core (Bahcall 1989). These methods have significantly contributed to our understanding of the internal dynamics of the Sun.

The quest to understand the formation of sunspots on the Sun has been a significant endeavor in solar physics. Historically, scientists have been attempting to predict the appearance of sunspots by tracking the rise of magnetic fields from the Sun's interior (Babcock 1961). Despite these efforts, accurately forecasting sunspot emergence has proven elusive. In a breakthrough, Ilonidis et al. (2011) have detected magnetic fields forming deep within the Sun by helioseismology, approximately 60,000 km beneath the surface, only one to two days before sunspots appear. Researchers detected a marked increase in the emergence rate of magnetic flux, which can cause a noticeable acceleration in the travel time of sound waves which serves as an indicator of an impending sunspot emergence. While this study offers a promising lead for space weather prediction and enhances our grasp of solar magnetic field dynamics, the precise timing and intensity of solar eruptions associated with sunspots still remain an open question.

Gravitational waves (GWs), as predicted by Einstein's theory of general relativity, were first detected in 2015 by the LIGO Scientific Collaboration and the Virgo Collaboration, marking a significant milestone in physics (Abbott et al. 2016). This direct observation confirmed a key prediction of general relativity and launched a new era of astronomical observation. GWs, unlike electromagnetic radiation, do not experience significant scattering or absorption as they propagate through the solar interior, making them an attractive tool for probing

¹ State Key Laboratory of Solar Activity and Space Weather, National Astronomical Observatories, Chinese Academy of Sciences, Beijing 100101, China; guansiqi22@mails.ucas.ac.cn, yangshb@nao.cas.cn

² School of Astronomy and Space Science, University of Chinese Academy of Sciences, Beijing 100049, China
³ School of Fundamental Physics and Mathematical Sciences, Hangzhou Institute for Advanced Study, University of Chinese Academy of Sciences, Hangzhou
310024, China; guoxiao17@mails.ucas.ac.cn

the internal structure of the Sun. This unique property allows for the potential detection of previously inaccessible regions within the solar convection zone and tacholine. GWs, unimpeded by solar plasma, offer a novel probe: solar magnetic flux emergence generates GWs via quadrupole moments, which could provide a new avenue for fundamental research into solar dynamics. Kokkotas & Schmidt (1999) pointed out that the detection of GWs produced by solar oscillations or magnetic activity, if detected, could provide valuable information about the Sun's interior structure and dynamics. The potential of GWs for solar interior probing has been highlighted in several theoretical frameworks (Hanasoge et al. 2012). The propagation of GWs in the solar medium has been extensively studied, with recent advancements in numerical simulations providing insights into the behavior of these waves within the context of solar dynamics (Brdar et al. 2019). Takahashi et al. (2023) propose leveraging lensed GWs from pulsars to probe solar density, bypassing limitations of intrinsic solar GW detection and traditional methods. Garcia-Cely & Ringwald (2025) calculate the complete GW spectrum generated by solar interior plasma, encompassing both microscopic (particle collisions) and macroscopic (hydrodynamic fluctuations) mechanisms. It assesses their detectability and contribution to the high-frequency GW background. These studies suggest that GWs could offer a novel perspective on the deep interior of the Sun, complementing traditional helioseismic methods.

Note that asymmetric magnetic flux emergence produces a non-zero gravitational quadrupole moment, generating detectable GWs. The Sun's proximity offers a unique detection opportunity, yet quantitative GW estimates from emerging flux tubes are scarce—particularly for predicting super active regions vital to space weather (Wang et al. 2009). This study aims to fill this theoretical gap by providing a first-order model and estimate, which is valuable for understanding the energetics of solar active regions. In this study, we model flux tubes as catenary curves—a geometry motivated by force equilibrium by using observational parameters of emerging solar active regions in solar cycle 23-24. We estimate the intensity of GWs generated during magnetic flux emergence and explore the potential for detection by GW observatories. In Section 2, we introduce the single-source oscillation model, adopting the catenary model to simplify the shape of magnetic flux tubes. Through quasi-static and magnetic flux conservation assumptions, we derive an equivalent density. The results are then discretized and incorporated into the single-source oscillation GW model, ultimately obtaining the amplitudefrequency relationship of GWs. In Section 3, we discuss the detectability of estimated GWs by detectors at different locations based on the estimated GW strength, and also consider the detectability after signal superposition.

2. Modeling and Results

2.1. Single-source GW Model

Within the framework of general relativity, the generation of GW requires that the second order derivative of the mass quadrupole moment \ddot{Q}_{ii} must be non-zero. The emergence process of magnetic flux tubes in the solar interior perfectly satisfies these conditions—the upward motion of flux tubes from the convection zone (approximately $0.75R_{\odot}$) to the photosphere exhibits significant spatial asymmetry, while the acceleration driven by magnetic buoyancy $(d^2r/dt^2 \sim B_{\phi}^2/(4\pi\rho r^2))$ produces strongly time-varying quadrupole moments. Moreover, radial density gradients $(\nabla \rho)$ in the plasma further amplify quadrupole variations. The quadrupole moment holds central importance in GW detection: the wave amplitude $h \propto |\ddot{Q}_{ii}|/(c^4r)$ directly depends on the quadrupole change rate, representing the dominant non-zero multipole order for gravitational radiation and carrying crucial information about the source's internal dynamics.

The theoretical foundation of GW generation lies in the quadrupole formula, which relates wave amplitude to the second time derivative of the mass quadrupole moment. For GWs propagating through spacetime, the transverse-traceless (TT) gauge amplitude is expressed as:

$$h_{ij}^{\mathrm{TT}}(t, \mathbf{x}) = \frac{1}{r} \frac{2G}{c^4} \Lambda_{ij,kl}(\hat{\mathbf{n}}) \ddot{Q}_{kl}(t - r/c)$$
 (1)

in which r denotes the source-observer distance; G and c represent the gravitational constant and speed of light respectively; $\Lambda_{ij,kl}$ is the projection tensor enforcing TT conditions; \ddot{Q}_{kl} signifies the second time derivative of the reduced quadrupole moment:

$$Q^{ij} = \int \rho(\mathbf{x}) \left(x^i x^j - \frac{1}{3} r^2 \delta^{ij} \right) d^3 x. \tag{2}$$

This fundamental relationship connects the dynamics of massenergy distributions with spacetime curvature perturbations.

The GW polarization amplitudes h_+ and h_\times are derived from the second time derivative of the reduced quadrupole moment $\ddot{\mathcal{Q}}^{ij}$ (defined in Equation (2)). However, in practical calculations, it is often convenient to work with the second mass moment M^{ij} :

$$M^{ij} = \int \rho(\mathbf{x}) x^i x^j d^3 x.$$

The reduced quadrupole moment Q^{ij} is related to M_{ij} by:

$$Q^{ij} = M^{ij} - \frac{1}{3}\delta^{ij}M_k^k,$$

where $M_k^k = \text{Tr}(M)$ is the trace of the mass moment tensor. For GW generation, only the trace-free part of M^{ij} contributes to radiation, which is exactly Q_{ii} .

GWs manifest through two polarization modes, h_+ and h_{\times} , whose amplitudes depend on the wave propagation direction

relative to the source orientation. For propagation along the z-axis $(\hat{n} = \hat{z})$, the polarization components simplify to:

$$h_{+} = \frac{1}{r} \frac{G}{c^4} (\ddot{M}_{11} - \ddot{M}_{22}), \tag{3}$$

$$h_{\times} = \frac{2}{r} \frac{G}{c^4} \ddot{M}_{12}. \tag{4}$$

For arbitrary propagation directions $\hat{n} = (\sin \theta \cos \phi, \sin \theta \sin \phi, \cos \theta)$, the complete angular dependence is described by:

$$h_{+}(t;\theta,\phi) = \frac{G}{c^{4}r} [\ddot{M}_{11}(\cos^{2}\phi - \sin^{2}\phi\cos^{2}\theta) + \ddot{M}_{22}(\sin^{2}\phi - \cos^{2}\phi\cos^{2}\theta) - \ddot{M}_{33}\sin^{2}\theta - \ddot{M}_{12}\sin 2\phi(1 + \cos^{2}\theta) + \ddot{M}_{13}\sin\phi\sin 2\theta + \ddot{M}_{23}\cos\phi\sin 2\theta], \quad (5)$$

$$h_{\times}(t;\theta,\phi) = \frac{G}{c^{4}r} [(\ddot{M}_{11} - \ddot{M}_{22})\sin 2\phi\cos\theta + 2\ddot{M}_{12}\cos 2\phi\cos\theta - 2\ddot{M}_{13}\cos\phi\sin\theta + 2\ddot{M}_{23}\sin\phi\sin\theta]. \quad (6)$$

These expressions fully characterize the wave's angular dependence and polarization states for arbitrary source configurations.

Following Hanasoge (2008)'s formulation of convective elements as vertically oscillating mass sources, we similarly model emerging magnetic flux tubes as point masses undergoing acceleration along the radial direction. This approach reduces complex magnetohydrodynamic processes to an analytically tractable quadrupole moment \ddot{Q}_{zz} (in Hanasoge's notation) or \ddot{Q}_{33} (in our notation), enabling efficient amplitude estimation. To model GWs from emerging solar magnetic flux tubes, we approximate a flux tube element as a point mass oscillating along the y-axis. The density distribution is described by:

$$\rho(t, \mathbf{x}) = \mu(t)\delta(x)\delta(z)\delta(y - y_0(t)),\tag{7}$$

where $\mu(t)$ represents the effective mass and $y_0(t)$ is its time-dependent position. This simplification preserves essential dynamics while rendering the quadrupole moment tractable. The resulting mass moment is:

$$M^{ij} = \mu(t) y_0^2(t) \delta^{i3} \delta^{j3}. \tag{8}$$

Substitution into polarization equations produces axisymmetric waveforms:

$$h_{+} = -\frac{1}{r} \frac{G}{c^4} \ddot{M}_{33} \sin^2 \theta, \tag{9}$$

$$h_{\times} = 0. \tag{10}$$

The amplitude scaling $h \sim \dot{M}_{33}/r$ reveals two critical aspects for detection: (1) the requirement for strong accelerations in dense plasma regions, and (2) the advantage of proximity to the source. These insights guide our subsequent

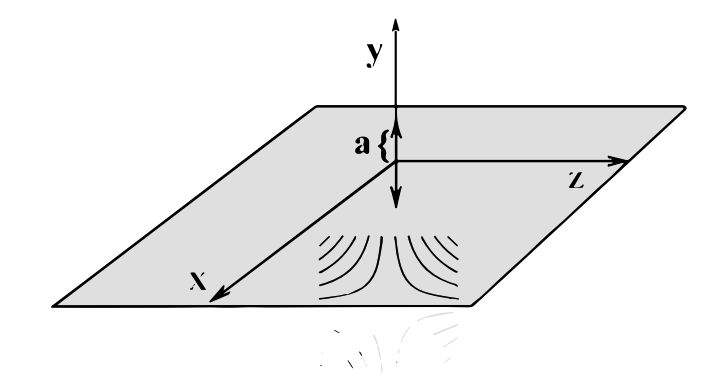


Figure 1. GW model for single-source: the source oscillating along the *y*-axis (double arrow), and the transverse stretching—compressing mode of the GW in the direction of $\theta = \frac{\pi}{2}$ (schematic of field lines), a represents the amplitude. Source: Maggiore (2008).

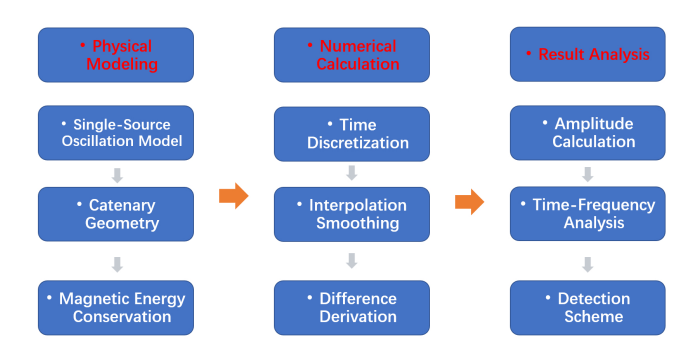


Figure 2. Flowchart of the gravitational wave estimation framework

analysis of solar GW detectability. Figure 1 illustrates the physical configuration and resulting wave pattern. The axisymmetric nature originates from cylindrical symmetry in the quadrupole moment generated by motion along a single axis. This simplified model establishes the foundation for estimating GWs from solar magnetic flux emergence, where complex dynamics are reduced to an effective vertical oscillation.

After introducing the single-source GW model in this study, Figure 2 illustrates the logical flow of our estimation approach. First, we build the physical model, in which the upward movement of solar magnetic flux tubes is simplified as a cluster of catenary curves with fixed endpoints. The geometric parameters are determined by the intersection coordinates of the catenary equation with the solar surface, and the equivalent density at different heights is derived using the principle of conservation of magnetic energy. Second, we present the numerical calculation process. The ascent of the emerging magnetic flux tube is discretized into several time steps, assuming the center point undergoes uniformly accelerated linear motion to obtain the displacement—time relationship. Finally, the result and analysis are presented. According to the single-source oscillation model used in this study, cubic spline

interpolation is used to smooth the data, and the central difference method is applied to calculate the second derivative of the mass quadrupole moment, thereby obtaining the spatiotemporal distribution of GW amplitude. This whole above process transforms complex magnetohydrodynamic processes into a computable quadrupole radiation model through catenary geometry, magnetic energy conservation, and motion discretization.

In the following subsection, Section 2.2 shows that how we adopt a catenary curve model to capture the quasi-static ascent of magnetic flux tubes. Section 2.3 is to derive the equivalent density profile by following the geometric setup. Sections 2.4 and 2.5 describe how to apply the motion discretize and compute the quadrupole moment. Section 2.6 shows the results of estimated GW amplitude and the time–frequency spectrograph.

2.2. Catenary Model of Flux Geometry

The adoption of the catenary geometry and the subsequent simplification of the flux tube motion to a uniformly accelerated ascent rely on two key physical assumptions: the quasi-static nature of the rise and the dominance of magnetic forces leading to nearly constant acceleration. These approximations are justified within the context of solar interior conditions and are supported by established magnetohydrodynamic (MHD) principles.

The rise of magnetic flux tubes through the solar convective zone is characterized by an extremely high magnetic Reynolds number $(R_m \sim 10^{11})$, a dimensionless parameter that quantifies the dominance of magnetic convection over diffusion. This condition indicates that the magnetic field is perfectly "frozen" into the highly conductive plasma on the emergence timescales considered in this study, satisfying Alfvén's frozen-in theorem. This physical regime justifies the treatment of the ascent within the framework of a quasi-static assumption. The core of this approximation lies in the clear separation of timescales. The characteristic rise time $(\tau_{\rm rise} \sim {\rm days})$ is significantly longer than the Alfvén time $(\tau_{\rm A} = L/v_{\rm A} \sim {\rm hours})$, the timescale required for the flux tube to establish mechanical equilibrium internally and with its surroundings:

$$\tau_{\rm rise} \gg \tau_{\rm A}$$
. (11)

This disparity implies that the flux tube evolves through a series of near-equilibrium states, rendering the inertial term $(\rho Dv/Dt)$ in the momentum equation negligible. Consequently, the dynamics are governed by a sequential static force balance at each point in the ascent:

$$0 \approx -\nabla p + \frac{1}{4\pi} (\nabla \times \mathbf{B}) \times \mathbf{B} + \rho \mathbf{g}_{\text{eff}}.$$
 (12)

This system of equations, coupled with the induction equation under the frozen-in flux condition, defines the quasi-static rise path of the flux tube. It is this foundational equilibrium that

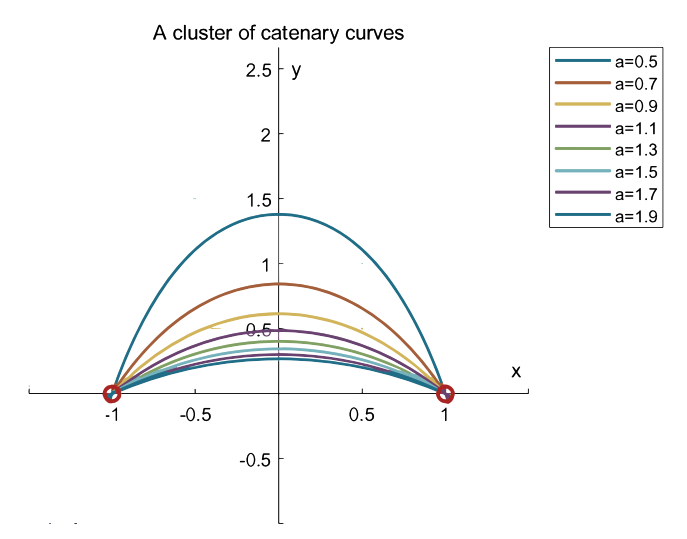


Figure 3. The figure illustrates a cluster of downward-opening catenary curves, sharing coincident *x*-axis intersections, as an approximation to the two-dimensional magnetic flux tube model.

validates the use of a static catenary geometry to model the flux tube's shape at each instance during its ascent in our analysis. The catenary geometry provides a mathematically tractable framework for flux tube ascent. In this study, the process of solar magnetic flux emergence is simplified to the emergence of a single catenary from the solar convection zone (at a depth of $0.75R_{\odot}$) to the solar surface (at the solar radius). The analysis is confined to a two-dimensional scenario, considering only the x and y axes, to examine the behavior of a single magnetic flux tube within a solar active region over a period of 30 days to emerge (Fan et al. 1993). In this paper, the emerging magnetic flux tubes in two-dimensional coordinates are simplified as a cluster of infinitely many catenary curves as Figure 3. The core of the catenary model lies in the exact mathematical correspondence between its differential equation form and the equilibrium equations of magnetic flux tubes. The classical catenary equation describes the static equilibrium of a flexible chain in a uniform gravitational field:

$$\frac{d^2y}{dx^2} = \frac{1}{a}\sqrt{1 + \left(\frac{dy}{dx}\right)^2},\tag{13}$$

in which a represents the ratio of tension to linear density. The catenary model of magnetic flux tube in the Sun is shown in Figure 4. The process of magnetic flux emergence from the solar convection zone to the photosphere is approximated as the vertical rise of a single catenary from the bottom of solar convective zone to the solar surface. The vertex of the catenary, where it intersects the y-axis, is determined based on the average height of sunspots above the photosphere, which is estimated to be at a position $(0, 1.125R_{\odot})$, where R_{\odot} is the solar radius. The standard catenary equation involves two

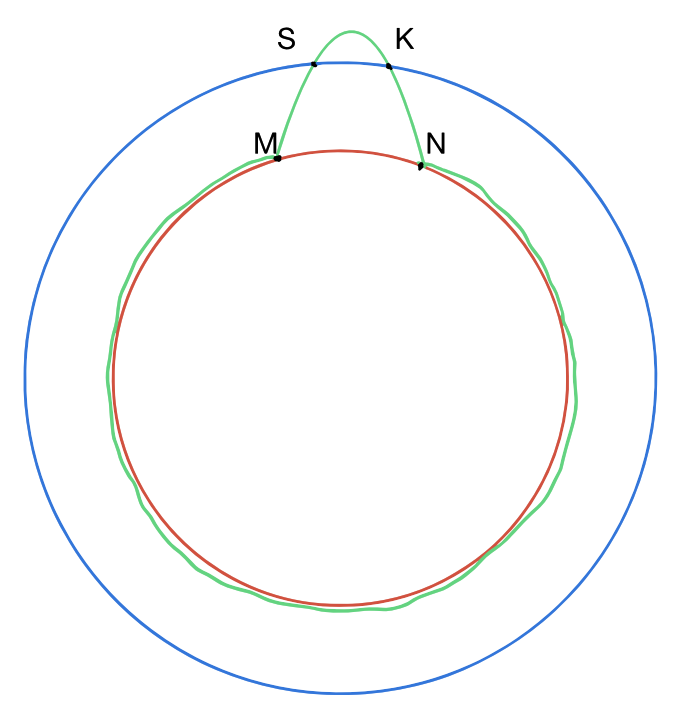


Figure 4. Catenary model. Here the red line represents bottom of convection zone, the green line represents the most marginal catenary, and the blue line represents the solar surface.

unknowns:

$$y = -a(t) \left[\frac{e^{\frac{x}{a(t)}} + e^{\frac{-x}{a(t)}}}{2} \right] + b(t), \tag{14}$$

thus necessitating an additional condition for its full determination.

This condition is provided by the arc length between two points, (0, R) and K: (p, q), on the catenary. The arc length is inferred from the radius of the active region and is approximated to be about AL₀ (Antiochos & McClymont 1982)

$$\int_{0}^{p} \sqrt{R^2 - x^2} dx = AL_0.$$
 (15)

With these parameters, we can derive the abscissa of K, then we substitute it into the equation of the solar surface, can we get the exact point K. Then the equation of the catenary at the vertex can be resolved, providing a mathematical description of the magnetic flux tube's shape as it emerges into the solar atmosphere.

2.3. Density Derivation

Under the above catenary geometry setup, we then need to estimate the density in the magnetic flux tube to further calculate the density derivation. First, we put forward the assumption of energy conservation, and its verification is as follows: The magnetic Reynolds number R_m , as a dimensionless parameter characterizing the coupling strength between

the magnetic field and fluid motion, is defined as the ratio of magnetic convection effect to diffusion effect: $\frac{UL}{\eta}$, where $U \sim 10^3 \, \mathrm{m \, s^{-1}}$ represents the typical convective velocity; $L \sim 10^8 \, \mathrm{m}$ represents the characteristic length of the magnetic flux tube (comparable to the active region scale); $\eta = \frac{1}{\mu_0 \sigma} \sim 1 \, \mathrm{m^2 \, s^{-1}}$ represents the magnetic diffusivity in the solar convective zone. In the solar convective zone $(R \approx 0.7 R_{\odot})$, $R_m \sim 10^{11}$, and the magnetic field is "frozen" into the plasma, satisfying the Alfvén's frozen-in theorem:

$$\frac{\partial \mathbf{B}}{\partial t} = \nabla \times (\mathbf{v} \times \mathbf{B}). \tag{16}$$

In this case, the magnetic flux through any material surface is conserved. Although the classical diffusivity η_{turb} is negligible, turbulent motions in the solar convective zone may introduce an effective magnetic diffusion effect. Using mixing-length theory to estimate the turbulent diffusivity: $\eta_{\rm turb} \approx 0.1 v_{\rm turb} l_{\rm turb} \sim 10^{-3} \, {\rm m}^2 \, {\rm s}^{-1}$, and the corresponding magnetic flux decay time is much longer than the flux tube rise time. This order-of-magnitude difference confirms that in single flux tube emergence events, the destruction of magnetic flux conservation by turbulent diffusion can be regarded as a higher-order small quantity. If magnetic reconnection events are considered, when the magnetic field gradient $\nabla B > 0.1 \,\mathrm{T\,m^{-1}}$, current sheet formation leads to local reconnection with a magnetic flux loss rate of approximately 5%. In this paper, this point is neglected, and it is still considered that the magnetic flux is approximately conserved during the rise of magnetic flux tubes in the solar interior. By invoking the assumption of conservation of magnetic energy in the vertical direction, we acknowledge that the magnetic energy present in the photosphere is:

$$E_s^0 = S_{\text{spots}} \cdot 2L_{\text{pho}}^H \cdot \frac{B_{\text{pho}}^2}{2\mu_0},\tag{17}$$

in which $S_{\rm spots}$ is the area of a hemisphere of a sunspot activity region, which can also be written as πp^2 (in which, p represents the radius of the sunspot. Here we adopt 5000 km as the sunspot radius for moderately active regions.), $\mu_0 = 4\pi \times 10^{-7}\,{\rm N\,A^{-2}}$, $L_{\rm pho}^H$ is the semidiameter of the catenary at the solar photospheric level, and $\frac{B_{\rm pho}^2}{2\mu_0}$ is the magnetic energy density within the photosphere. Second, we acknowledge that the magnetic energy present in any time is:

$$E_s^0 = 2L^H(t) \cdot \pi \omega_d^2 \cdot \frac{B_E^2}{2\mu_0},$$
 (18)

in which $\pi\omega_d^2$ is the area defined by the radii corresponding to the *x*-coordinates of the intersection points of each catenary with a circle, $L^H(t)$ is the semidiameter of the catenary at any given time t, and $\frac{B_E^2}{2\mu_0}$ is the magnetic energy density of the

corresponding time. Solving the two aforementioned magnetic energy equations simultaneously yields:

$$B_E^2 = \frac{p^2 \cdot 580\pi \cdot B_{\text{pho}}^2}{L^H(t) \cdot \omega_d^2}.$$
 (19)

According to mass energy equation: $E=mc^2=\rho\cdot V\cdot c^2=V\cdot \frac{B_E^2}{2\mu_0},$ we can yield:

$$\rho = \frac{B_E^2}{2\mu_0 c^2}. (20)$$

Let us substitute B_E^2 into the equation above:

$$\rho = \frac{p^2 \cdot 580\pi \cdot B_{\text{pho}}^2}{2L^H(t) \cdot \omega_d^2 \cdot \mu_0 c^2}.$$
 (21)

2.4. Motion Discretization

In this section, we discretize the entire emerging motion cycle of the magnetic flux tubes. To simplify the calculations, we further consider the rise of the magnetic flux tube as a uniform accelerated straight-line motion, thereby obtaining the displacement–time relationship s(t) for the center point of the magnetic flux tube. A time interval of 1000 s was selected to discretize the total duration of 30 days: $k=3600\times24\times30=2.592\times10^6$ s, resulting in 2592 distinct time steps. Consequently, there are 2592 instances of the catenary equation that need to be solved. As illustrated in Figure 4, all 2592 catenaries share the same endpoints, denoted as M and N, with the caveat that points M and N are symmetric with respect to the y-axis, thus constituting a single boundary condition. It is essential to determine the coordinates of the intersection of each catenary with the y-axis.

Referring to the literature by Fan (2021), the motion of magnetic flux tubes is governed by the magnetohydrodynamic (MHD) equations, which account for the combined effects of magnetic fields, plasma, and gravity. Assuming radial motion of the flux tube and axisymmetry ($\frac{\partial}{\partial \theta} = 0$), the equation simplifies to:

$$\rho \frac{d^2 r}{dt^2} = -\frac{\partial p}{\partial r} + \frac{B_{\phi}}{4\pi r} \frac{\partial (rB_{\phi})}{\partial r} + \rho g_{\text{eff}} - \frac{1}{r} \frac{\partial}{\partial r} (r\Pi_{rr}).$$
 (22)

Here, B_{ϕ} is the azimuthal magnetic field component, ρ is the plasma density, r is the radial position of the flux tube. This system incorporates contributions from the internal pressure gradient, magnetic field effects, and external effective gravity. Under magnetically dominant conditions, the pressure gradient and viscous terms become negligible, reducing the equation to: $\frac{d^2r}{dt^2} \approx \frac{B_{\phi}^2}{4\pi\rho r^2}.$ If the azimuthal magnetic field B_{ϕ} varies slowly with radius $(\frac{\partial B_{\phi}}{\partial r} \approx 0)$, the acceleration a approaches a constant

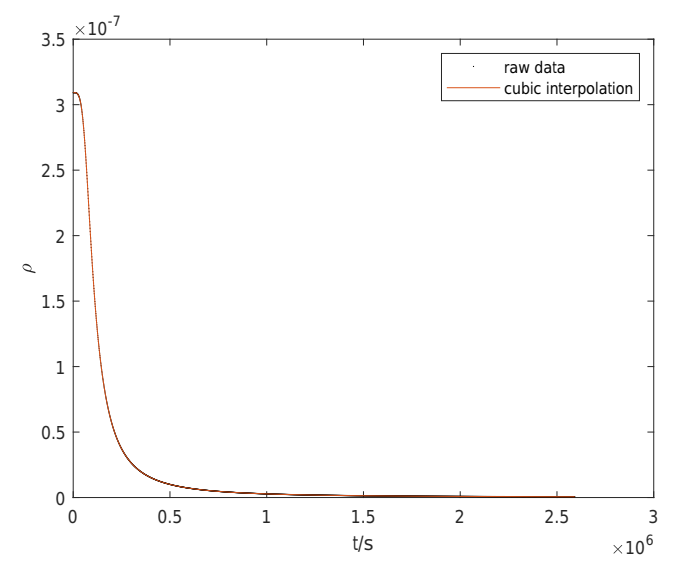


Figure 5. Temporal evolution of the equivalent density ρ during flux tube ascent. The orange curve is the cubic interpolation fitting curve based on the original data, and the 2591 black dots represent raw data points.

value, supporting the uniform acceleration hypothesis. Then the ascent of the catenary's central point is simplified to uniformly accelerated linear motion. The continuous motion equation of the catenary's midpoint can be derived from the duration of motion and the distance traveled as follows

$$s(t) = \frac{R}{2k^2} \left[k^2 e^{\frac{k-t}{k}} - 0.5t^2 \right] + \frac{R}{2k} \cdot et + (0.75 - 0.5e)R.$$
 (23)

Our approach involves further discretizing this motion into 2592 discrete points. This discretization also provides the second condition necessary for ascertaining the catenary equations. Thus we can discretize the catenary that rises along the *y*-axis as Equation (7) in which $y_0(t)$ is the 2592 interval time of s(t). Besides, it is obvious that in the process of the magnetic flux tube rising, only the "half-stroke" of the motion along the positive direction of the *y*-axis is considered in Figure 1.

Finally, we can get ρ of 2592 time intervals based on Equation (8). Construct a cubic polynomial function to approximate the unknown function between the data points, ensuring that the interpolation results are smooth and the derivatives are continuous in the adjacent intervals, which is achieved by using the cubic spline interpolation method. Figure 5 shows the temporal evolution of the equivalent density ρ during flux tube ascent.

Subsequently, we use the model in Section 2.1 to calculate the GW quadrupole moment for a single source oscillating along the *y*-axis in three-dimensional space (Maggiore 2008).

2.5. Quadrupole Moment Computation

The second mass moment is:

$$M^{ij} = \int \rho(t, x) x^i x^j d^3 x$$

$$= \int \rho(t, x) x^i x^j d^3 x$$

$$= \mu(t) y_0^2(t) \delta^{i3} \delta^{j3}$$

$$= \mu(y) s^2(t) \delta^{i3} \delta^{j3}.$$
(24)

Based on the symmetry relations, i.e., the geometric relation, it is obvious that there is only M^{33} left: $M^{33} = \mu_0(t)y_0^2(t) = \mu(y) \cdot y_0^2(t) = \rho(y) \cdot y_0^2(t) \cdot \frac{H_{\text{tot}}}{2592} \cdot \frac{W_{\text{tot}}}{2592}$ in which, H_{tot} represents for the total height of the ascending process: (1.125-0.75)R, W_{tot} represents for the total width of the ascending process

$$\begin{cases} M^{33} = \rho(t) \cdot y_0^2(t) \cdot \frac{(1.125 - 0.75)R}{2592} \cdot \frac{2m}{1000}, \\ y_0(t) = \frac{R}{2k^2} \left[k^2 e^{\frac{k \cdot t}{k}} - \frac{1}{2} t^2 \right] + \frac{R}{2k^2} \cdot ke \cdot t + \left(\frac{3}{4} - \frac{e}{2} \right) R, \\ k = 30 \times 3600 \times 24. \end{cases}$$
(25)

In numerical analysis, the second-order difference is used to approximate the second derivative of a function. It is an important tool in the discretization of differential equations and signal processing. Given a set of discrete points with equal step sizes $f_i = f(x_i)$, where $x_i = x_0 + ih$, the Taylor expansions of $f(x_{i+1})$ and $f(x_{i-1})$ are as follows:

$$f(x_{i+1}) = f(x_i) + hf'(x_i) + \frac{h^2}{2}f''(x_i)$$

$$+ \frac{h^3}{6}f'''(x_i) + O(h^4)$$

$$f(x_{i-1}) = f(x_i) - hf'(x_i) + \frac{h^2}{2}f''(x_i)$$

$$- \frac{h^3}{6}f'''(x_i) + O(h^4). \tag{26}$$

Add the two equations in equation to eliminate the first-order derivative terms

$$f(x_{i+1}) + f(x_{i-1}) = 2f(x_i) + h^2 f''(x_i) + O(h^4).$$
 (27)

We can then obtain $f''(x_i)$. That is, using the 2592 sample points M_{33} obtained from Equation (25), we substitute them into Equation (27) and use the central difference method to obtain 2591 values of the second derivative of mass moment \ddot{M}_{33} . Figure 6 shows the temporal evolution of \ddot{M}^{33} .

In addition, Table 1 presents the symbols used and their interpretations in this section.

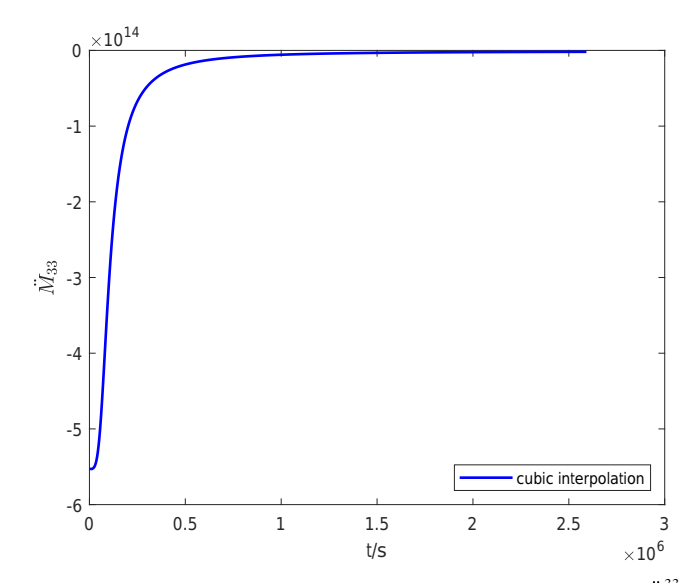


Figure 6. Temporal evolution of the second derivative of mass moment \ddot{M}^{33} . The blue curve is the cubic interpolation fitting curve based on the original data.

2.6. Results

Once M^{33} is given in last subsection, we are easily able to compute the angular distribution of the quadrupole radiation:

$$h_{+}(t; \theta, \phi) = -\frac{1}{r} \frac{G}{c^4} \ddot{M}^{33(tret)} \sin^2 \theta$$
$$= \frac{2G\mu a^2 \omega_s^2}{rc^4} \sin^2 \theta \cos(2\omega_s t_{\text{ret}}), \tag{28}$$

$$h_{\times}(t;\,\theta,\,\phi) = 0. \tag{29}$$

Here, r denotes the distance between the detector and the wave source, G is the gravitational constant, $G = 6.67430 \times 10^{-11} \,\mathrm{m}^3\,\mathrm{kg}^{-1}\,\mathrm{s}^{-2}$.

Based on GW strain signal Equation (28), we perform a Short-Time Fourier Transform (STFT) to obtain the time–frequency spectrogram in Figure 7. It intuitively displays the dynamic evolution of frequency components in GW signals over time. As shown in Figure 7, the frequency range is lower than 3×10^{-5} Hz, which is close to the Pulsar Timing Array (PTA) band (Bustamante-Rosell et al. 2022).

By integrating these profiles into our theoretical framework and assuming a detector at

$$r = 1 \text{ au}, \tag{30}$$

we derive a GW strain amplitude of

$$h \sim 10^{-42}$$
. (31)

This value is far below the detectability range of existing GW observatories. Notably, the characteristic frequency of GWs generated by solar emerging magnetic flux tubes—estimated herein to be 10^{-5} Hz (as the dominant component in Figure 7)—exhibits striking consistency with the sensitive frequency

Table 1Symbol Interpretation Table

	, 1
Symbol	Explanation
R_{\odot}	solar radius
k	total duration of single emergence cycle
t	time
s(t)	displacement-time relationship of the center point
e	nature exponential
$S_{ m spots}$	area of a hemisphere of a sunspot activity region
E_s^0	magnetic energy present in the photosphere
$L_{ m pho}^{H}$	semi-diameter of the catenary at the photosphere
μ_0	permeability of vacuum
$B_{ m pho}$	magnetic field intensity of photosphere
$L^H(t)$	semi-diameter of the catenary of time t
ω_d	radii corresponding to <i>x</i> -coordinates of intersection points of each catenary with a circle
B_E	magnetic field density of corresponding time
c	speed of light
ρ	density
m	mass
M^{ij}	second mass moment
H_{tot}	total height of ascending process
$\overline{W_{ m tot}}$	total width of ascending process
h_+	polarization component of + mode
$h_{ imes}$	polarization component of cross mode
$\overline{AL_0}$	arc length

band of the Cassini spacecraft, a landmark low-frequency GW detector. According to Armstrong (2006), Cassini conducted systematic GW observations via precision Doppler tracking during its 2001–2003 solar opposition campaigns, covering a frequency range of 10^{-6} – 10^{-3} Hz. This frequency alignment is not coincidental. Cassini's 10^{-6} – 10^{-3} Hz band was strategically designed to detect low-frequency GWs from astrophysical sources with spatial scales comparable to the Earth-spacecraft separation (1–10 au), which aligns with the physical scale of solar magnetic flux tube emergence (from solar radius to au-scale). Importantly, this consistency does not imply that Cassini directly detected GWs from solar flux tubes; rather, it confirms that our theoretically derived frequency falls within the validated range of mature low-frequency GW detection technologies, providing indirect observational support for the plausibility of our model—where GW generation is driven by

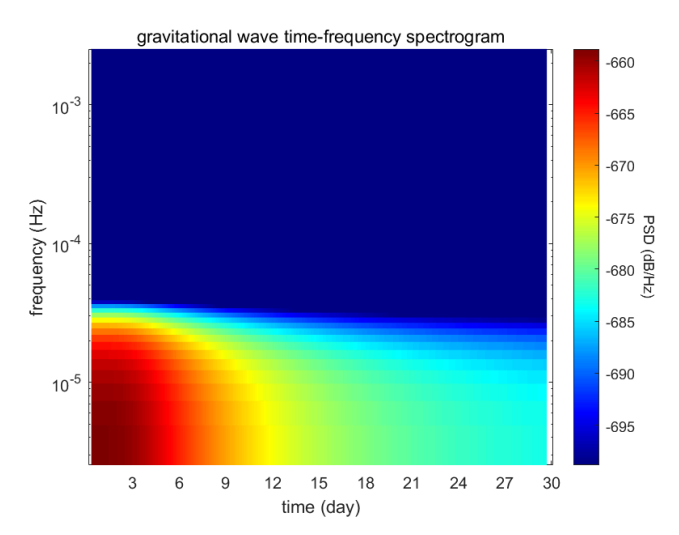


Figure 7. The time–frequency spectrogram obtained through STFT method, in which colors are used to represent the logarithmic power spectral density of the GW strain signal across time and frequency, illustrating the distribution of signal intensity.

the buoyancy of magnetic flux tubes. The superposition of signals from multiple flux tubes could potentially approach the detectability threshold for future high-precision GW observatories.

3. Discussion

To properly contextualize the significance of our estimated signal, it is essential to compare it not only in amplitude but also in character to the dominant sources of the stochastic gravitational wave background (GWB) in the nanohertz to microhertz regime (Xu et al. 2023; Agazie et al. 2023). The GWB in this frequency band is expected to be dominated by: (i) a cosmological component from processes such as inflation or phase transitions in the early universe, and (ii) an astrophysical component from the unresolved population of supermassive black hole binaries (SMBHBs; Sesana 2016).

The key distinction lies in their temporal properties. Both the cosmological and SMBHB backgrounds are modeled as stationary, Gaussian, and isotropic random processes. Their timescales are cosmological or galactic, spanning from years to the age of the universe ($\sim 10^7 - 10^{17}$ s), making them effectively constant over any realistic observational cadence (Amaro-Seoane et al. 2017; Maggiore 2018).

In stark contrast, the GW signal from solar magnetic flux emergence, as predicted by our model, is intrinsically transient and non-stationary. It is tied to discrete emergence events with a characteristic duration on the order of days. Crucially, its dominant oscillatory component has a period of ~ 1 day ($\sim 10^5$ s), as determined by the buoyant rise time.

This fundamental difference in timescales—cosmological $(\sim 10^{17} \text{ s})/\text{stellar-orbit}$ $(\sim 10^7 \text{ s})$ versus solar-dynamic $(\sim 10^5 \text{ s})$ —is the key to distinguishing a potential solar contribution. It implies

that the solar signal would be localized in time and manifest as a non-Gaussian, intermittent component superimposed on the smooth, stationary background. Advanced data analysis techniques, such as time-domain searches for transients or cross-correlation with solar activity proxies, could, in principle, leverage this timescale disparity to isolate the solar signature (Hanasoge et al. 2012; Bustamante-Rosell et al. 2022).

Therefore, while the solar GW strain is indeed weak, its unique and well-defined temporal signature means its contribution cannot be dismissed merely on the basis of amplitude. Our work provides a first physical prediction of this specific timescale and waveform, which is a necessary precursor to developing such targeted data analysis strategies.

Regarding the detectability of GWs, current ground-based detectors such as LIGO, Virgo, and KAGRA (Page et al. 2021) achieve their optimal strain sensitivity of approximately 10^{-23} in the frequency band of 50–300 Hz, where seismic noise and thermal noise are minimized. However, the value of 10^{-42} calculated in Section 2 is evidently insufficient for detection, indicating that the GW signals generated by the processes under consideration are too weak to be detected by existing ground-based detectors.

First, let us discuss the impact of detector location on the possibility of detection. In the previous section, we assumed that the detector is placed at a distance of one au from the Sun. Under this assumption, a single magnetic flux tube would generate GWs with an amplitude of 10^{-42} during a solar activity cycle. The Parker Solar Probe (PSP; Raouafi et al. 2023) can reach as close as 0.04 au to the Sun. If a future solar magnetic emergence GW detector could also reach such a close position, the GWs generated by a single magnetic flux tube over the entire solar activity cycle would have an amplitude of 10^{-40} .

Second, let us consider the effect of signal superposition. The detector will simultaneously detect the superimposed GW signals from all active regions and all magnetic flux tubes during a solar cycle. In a comprehensive review by Schmidt (1999), it is suggested that a moderate active region (AR) may contain on the order of $N \sim 10^3$ flux tubes, while a large, complex active region can host as many as $N \sim 10^5$. This disparity is attributed to the greater magnetic complexity and area of larger ARs, which can support a higher number of flux tubes. The combined strain amplitude from N independent sources scales as $h_{\text{total}} \sim h_{\text{single}} \cdot \sqrt{N}$. According to data from the Huairou Solar Observing Station, the average number of sunspots for 2024 August was 215, indicating a moderate level of solar activity. In the context of this study, the GW amplitude associated with the emergence of magnetic flux from the solar convection zone is estimated to be around 10^{-28} if the detector is located at around 0.04 au from the Sun simply like PSP (Raouafi et al. 2023). This estimation pertains to a single active region and a segment of the flux tube's emergence cycle.

Despite this significant amplification through both superposition and proximity, the resulting strain amplitudes must be contextualized against the sensitivity of relevant detectors. The current best sensitivity for PTAs in the nanohertz band is approximately ($h_c \sim 10^{-15}$). Even the most optimistic estimate above remains 12 orders of magnitude below this threshold. Notwithstanding this immense sensitivity gap, the unique frequency and directional nature of the signal warrant a discussion of the theoretical requirements for its detection via advanced methods such as PTAs or Gravitational Wave Timing Arrays (GWTAs). Therefore, we explicitly conclude that the detection of GWs from solar magnetic flux emergence, even under optimistic assumptions of signal superposition and advanced detector placement, presents an immense challenge that lies beyond the reach of current or near-future technology. The estimated GW frequency of $\sim 10^{-5}$ Hz places the signal at the high-frequency end of the PTA band and within the sensitivity range of GWTA concepts (Bustamante-Rosell et al. 2022). To robustly assess the detection challenge, it is crucial to evaluate the uncertainties inherent in our model, which arise primarily from three sources: (i) the photospheric magnetic field strength B_{pho} , (ii) the number of flux tubes N within an active region, and (iii) magnetic flux loss during ascent. In contrast to the previous simplified treatment, we now incorporate observational statistics to better capture the probabilistic nature of these parameters. We model the variability in B_{pho} using a truncated normal distribution centered at 4000 G with a standard deviation of 1000 G, reflecting the typical range of observed sunspot field strengths (Toriumi & Takasao 2017). Since the strain amplitude scales as $h \propto B_{\rm pho}^2$, this introduces a factor of ~ 2 uncertainty in amplitude. The number of flux tubes N per active region is highly variable. Based on solar active region classifications, we assign a probability distribution to N: small ARs $(N \sim 10^2 - 10^3)$ occur with probability 0.6, moderate ARs $(N \sim 10^3 - 10^4)$ with probability 0.3, and large/complex ARs $(N \sim 10^4 - 10^6)$ with probability 0.1 (Schüssler & Vögler 2008). This reflects the observed rarity of very large active regions. Since the combined strain scales as $h_{\text{total}} \propto \sqrt{N}$, this contributes a variability spanning two orders of magnitude. Magnetic flux loss due to reconnection and turbulent dissipation is parameterized by an efficiency factor η_B , which we model as a uniform distribution between 0.8 and 0.95, leading to a further scaling of $h \propto \eta_B^2$ (a factor of 0.64–0.90). Propagating these uncertainties jointly through a Monte Carlo analysis (10⁵ samples), we find that the overall strain amplitude (for a detector at 0.04 au) spans a 95% confidence interval of:

$$h_{\rm total} \sim 10^{-31}$$
 to 10^{-27} .

This range remains 12 to 16 orders of magnitude below current PTA sensitivities ($h_c \sim 10^{-15}$), underscoring the profound challenge of detection. Our refined analysis highlights the

importance of incorporating solar active region statistics into future estimates and provides a more realistic uncertainty quantification for this emission mechanism. According to the fundamental principle of PTA detection, (Guo, Lu & Yu 2022). The observable frequency range is intrinsically determined by the observational cadence. The maximum detectable frequency $f_{\rm max}$ satisfies the Nyquist criterion: $f_{\rm max} \leqslant \frac{1}{2\Delta t}$, where Δt is the cadence, which means time interval between successive observations. Conventional PTA observations typically employ cadences of weeks to months, which limits their sensitive band to the nanohertz regime. However, the GW signals from solar magnetic flux emergence are predicted to peak near 10^{-5} Hz. To access this higher frequency band, the observational cadence must be significantly shortened. Reducing the sampling interval from the typical two-week cadence to approximately two hours $(\Delta t = 2 \text{ hr})$ would raise the maximum detectable frequency to about 5.8×10^{-5} Hz, thereby encompassing the dominant spectral component of solar activity-related GWs. This highcadence strategy would not only improve the frequency coverage but also enhance the capability to resolve the temporal evolution of these transient signals, potentially facilitating their separation from the stationary stochastic background. For a detection via PTA, the signal-to-noise ratio scales as:

$$SNR \approx h \sqrt{N_p Tf} / \sigma_t, \tag{32}$$

where $h \sim 10^{-28}$ is the strain amplitude after superposition, N_p is the number of pulsars, T is the integration time, f is the GW frequency, and σ_t is the timing precision. A detectable SNR \gtrsim 5 would require timing precisions at the level of 100 fs or better, achievable with future facilities like the Square Kilometre Array, along with a network of ~50-200 millisecond pulsars sampled at hourly cadence over 6 months to 2 yr. For GWTA, which leverages phase modulation of Galactic binary signals observed by LISA, the weak modulation amplitude $\Delta\Phi \sim 10^{-26} \, \mathrm{rad}$ per source necessitates stacking $\sim 10^3 - 10^4$ sources over 5–10 yr to reach a detectable collective signal. These requirements are consistent with projected capabilities of next-generation detectors, underscoring the feasibility of both methods in principle, though formidable practical challenges remain. The primary value of this estimate is not to claim detectability but to provide a firstorder quantitative benchmark for this specific solar GW emission mechanism. It establishes an upper bound and informs future theoretical studies on the contribution of stellar activity to the millihertz gravitational-wave foreground.

The implications of these findings may be profound. The detection and measurement of GWs from solar activity can provide invaluable insights into the dynamics of the solar interior and the processes that drive solar magnetism. Furthermore, our study invites speculation about a long-term scientific vision: understanding the radiation mechanism of solar GWs may ultimately provide a novel, independent

physical probe for studying the accumulation and release of magnetic energy within the Sun. However, it is crucial to emphasize that this would only become possible if a profoundly deep understanding of the physical connection between magnetic flux tube emergence and solar surface activity (e.g., flares, coronal mass ejections) is achieved, and routine, real-time detection of its GW signal is realized. Even then, it could only potentially provide valuable, complementary input for space weather models. The core value of the current work lies in establishing the theoretical foundation and providing quantitative estimates, paving the way for this distant possibility in the future. As our detection capabilities improve, we can expect to gain a clearer picture of the complex dance of magnetic fields within our Sun.

It should be noted that these estimates are based on current models and observations. Future observations and advancements in observational technology may provide more precise data, which could further refine our understanding of solar interior structure.

In addition, in practical detection, it is necessary to pay attention to the influence of solar background GWs, flares, and other factors. The shape of the magnetic flux tube is also not in a standard linear form. These limitations require rigorous corrections in future studies. In the future, three-dimensional numerical simulations will be used to conduct rigorous estimates of GWs from solar internal magnetic emergence.

Acknowledgments

We would like to thank the referee for carefully reading our manuscript and for giving constructive comments that substantially helped improving the paper. This research is supported by the Strategic Priority Research Program of the Chinese Academy of Sciences (grant No. XDB0560000); by the National Key R&D Program of China Nos. 2022YFF0503800, 2021YFA1600500 and 2022YFF0503001; by the National Natural Science Foundation of China (grant No. 12250005); by the CAS funding GJ11020403-1; and by the Chinese Meridian Project (CMP). X.G. is supported by the Postdoctoral Fellowship Program and China Postdoctoral Science Foundation under grant No. BX20230104.

ORCID iDs

References

Abbott, B. P., Abbott, R., Abbott, T. D., et al. 2016, PhRvL, 116, 061102 Agazie, G., Anumarlapudi, A., Archibald, A. M., et al. 2023, ApJL, 951, L8 Amaro-Seoane, P., Audley, H., Babak, S., et al. 2017, arXiv:1702.00786 Antiochos, S. K., & McClymont, A. N. 1982, SoPh, 78, 153 Armstrong, J. W. 2006, LRR, 9, 1 Babcock, H. W. 1961, ApJ, 133, 572

```
Bahcall, J. N. 1989, Neutrino Astrophysics (Cambridge: Cambridge Univ. Press)
Brdar, V., Helmboldt, A. J., & Kubo, J. 2019, JCAP, 2019, 021
Bustamante-Rosell, M. J., Meyers, J., Pearson, N., Trendafilova, C., & Zimmerman, A. 2022, PhRvD, 105, 044005
Xu, H., Chen, S., Guo, Y., et al. 2023, RAA, 23, 075024
Fan, Y. 2021, LRSP, 18, 5
Fan, Y., Fisher, G. H., & DeLuca, E. E. 1993, ApJ, 405, 390
Garcia-Cely, C., & Ringwald, A. 2025, PhRvL, 135, 061001
Gizon, L., & Birch, A. C. 2005, LRSP, 2, 1
Guo, X., Lu, Y., & Yu, Q. 2022, ApJ, 939, 55
Hanasoge, S. M. 2008, ApJ, 680, 1457
Hanasoge, S. M., Duvall, T. L., Jr., & Sreenivasan, K. R. 2012, PNAS, 109, 11928
Ilonidis, S., Zhao, J., & Kosovichev, A. 2011, Sci, 333, 993
```

```
Kokkotas, K. D., & Schmidt, B. G. 1999, LRR, 2, 1
Maggiore, M. 2008, Gravitational Waves: Vol. 1, Theory and Experiments (Oxford: Oxford Univ. Press)
Maggiore, M. 2018, Gravitational Waves: Vol. 2: Astrophysics and Cosmology (Oxford: Oxford Univ. Press)
Page, M. A., Goryachev, M., Miao, H., et al. 2021, CmPhy, 4, 27
Raouafi, N. E., Matteini, L., Squire, J., et al. 2023, SSRv, 219, 8
Schmidt, M. 1999, ApJL, 523, L117
Schüssler, M., & Vögler, A. 2008, A&A, 481, L5
Sesana, A. 2016, PhRvL, 116, 231102
Takahashi, R., Morisaki, S., & Suyama, T. 2023, ApJ, 957, 52
Toriumi, S., & Takasao, S. 2017, ApJ, 850, 39
Wang, J., Yan, Y., Aschwanden, M. J., & Wang, H. 2009, SoPh, 258, 227
```